CoOx-caged Metal-organic Frameworks for Sonocatalyzing CO_2 to CO for Ultrasound-assisted Chemodynamic-Gas Cancer Therapy

Tian Zhang[1, ‡], Qiang Zheng[2, ‡], Jie Huang[4], Xiang Li[1,3*]*

[1] State Key Laboratory of Silicon and Advanced Semiconductor Materials, School of Materials Science and Engineering, Zhejiang University, Hangzhou 310058, China.

[2] Key Laboratory of Endoscopic Technique Research of Zhejiang Province, Sir Run Run Shaw Hospital, Zhejiang University, Hangzhou 215123, P. R. China

[3] ZJU-Hangzhou Global Scientific and Technological Innovation Center, Zhejiang University, Hangzhou, 311200, P.R. China.

[4] Department of Mechanical Engineering, University College London, London WC1E 7JE, UK

* Corresponding Author: jie.huang@ucl.ac.uk; xiang.li@zju.edu.cn (XL)

‡ Authors with equal contribution

Abstract: Carbon monoxide (CO) as one of the endogenous gaseous signaling molecules, has been widely studied to inhibit cancer cell proliferations for Gas Therapy. However, the therapeutic efficiency of CO gas therapy is far from ideal due to the low availability of CO supply. Here, inspired by the band structure and Fenton-related elements, MIL-101(Cr)@CoOx nanoparticles were introduced for the first time to achieve ultrasound-mediated synergistic therapy by combining CO gas therapy and chemodynamic therapy (CDT) together effectively. MIL-101(Cr)@CoOx could present substantial CO_2 adsorption capacity for the BDC^{2-} linkers and Co center, and enable to transform endogenous CO_2 to CO efficiently under ultrasound irradiation due to the appropriate band structure and conduction band position. With the Co-engaged Fenton-like reaction, MIL-101(Cr)@CoOx triggered the reactions to catalyze the over-expressed intracellular H_2O_2 into cytotoxic hydroxyl radicals ($\cdot$OH). We demonstrated that the potential therapeutic outcome of chemodynamic therapy could be amplified by the ultrasonic cavitation-induced conversion between Co^{3+} and Co^{2+} in vitro. The proliferations, ATP and mitochondria functions of 4T1 mouse breast cancer cells were severely compromised by CO-promoted ROS generation and sono-Fenton effect. Further in vivo studies confirmed that MIL-101(Cr)@CoOx combining with ultrasound irradiation exhibited superior tumor suppression, and achieved the ultrasound-mediated chemodynamic-gas cancer therapy with higher precisions for personalized treatments. This new system developed offers a distinct concept to construct smart ultrasound-stimulus systems to realize synergetic cancer therapy.

1. Introduction

Cancer is a leading cause of death worldwide, accounting for nearly one in six deaths in 2020 (World Health Organization), apposing an enormous threat to human health. While conventional treatments suffer limited efficiency due to drug resistance, postoperative recurrence, the systemic toxicity and nonspecificity[1], gas therapy, utilizing physiologically signaling gases (i.e. carbon monoxide, nitric oxide, hydrogen sulfide and hydrogen), has gained increasing attentions in treating inflammation-related diseases[2], such as cancer in particular. These endogenous gaseous signaling molecules are the critical messengers in regulating anti-inflammatory and anti-oxidative reactions in physiological and pathophysiological processes[3] Previous studies found that carbon monoxide (CO) could cause mitochondrial dysfunction, reduce cellular energy and promote the production of reactive oxygen species (ROS), thus leading to cancer cell apoptosis[4]. At the concentration of 250 ppm, CO could inhibit cancer cell proliferation effectively [5]. CO could also inhibit the activity of enzymes, such as cystathionine b-synthase (CBS) [6]. However, the direct use of CO presents clear drawbacks including toxic effect, low bioavailability and uncontrolled diffusivity[7]. A series of advanced systems, such as stimulus-responsive (H_2O_2, light etc.) CO donors and CO-carrying nanoplatforms, have been explored to deliver CO-releasing molecules (CORM) in an indirect manner[8]. Poor CO loading efficacy and systemic toxicity remain challenging for its potential clinical applications.

Recently, Zhang and the coworkers utilized the intratumoral high level of CO_2 (pCO_2 = 80 mmHg) and constructed a photo-catalyst (histidine-rich peptide modified Ag_3PO_4 doped carbon-dot-decorated C_3N_4 nanoparticles, HisAgCCN), which was able to convert endogenous CO_2 to CO, and achieve a combination of targeted CO gas therapy with chemotherapy[9]. The generation of CO was

driven by the amino acid-governed enhanced CO_2 collection, and the reduction mechanisms of CO_2 was based on the Z-scheme Type Heterogeneous system under 630 nm laser irradiation[9b]. However, the limited penetration depth of light hinders its therapeutic efficiency [10]. Owing to its nondestructive and deep-penetration nature, ultrasound has been widely investigated in sonodynamic and sono-assisted tumor therapies[11]. Various sonosensitizers have been studied, such as porphyrins organic compounds, some small-molecule agents (IR780 and ICG, etc.) and inorganic semiconductors[3a]. The semiconductors could adsorb ultrasound energy from sonoluminescence driven by the ultrasonic cavitation process. The electrons on the valence band are excited to the conduction band, and activated electrons and holes are formed. Depending on the band structure and the edge of the semiconductors[12], the sono-generated electrons or holes then react with reactants in the environment and enable redox reactions. Therefore, it appears to be feasible to realize an ultrasound-assisted catalytic conversion of CO_2 to CO.

A number of studies have favored combinations of cancer therapies for higher efficiency [2a]. It is expected that the effectiveness of CO gas therapy could be further enhanced due to the combination with other therapies, especially ROS-related approaches. Chemodynamic therapy (CDT), presenting advantages of minimal invasiveness and high tumor specificity, is enabled by the conversion of over-expressed hydrogen peroxide (H_2O_2) into hydroxyl radical ($\cdot$OH), the most harmful reactive oxygen species (ROS) inducing cell apoptosis and necrosis[13]. The CDT effectiveness could be enhanced due to mitochondrial dysfunction and ROS production resulted from CO[14]. Various transition metal elements-containing agents/materials such as iron (Fe), cobalt (Co), copper (Cu) and manganese (Mn) have been widely investigated as CDT agents[15]. They could intelligently respond to internal or/and

external stimulus and release relevant ions with high catalytic activity for Fenton or Fenton-like reaction[16]. Nevertheless, the therapeutic efficiency is limited by the strict reaction conditions (pH, H_2O_2 etc.) and the insufficient release of crucial metal ions. Ultrasound and near-infrared (NIR) light have been utilized to effectively promote Fenton reactions and boost treatment outcomes of CDT[17]. Ultrasound with cavitation effects can enhance the matter transfer and agitate chemical reactions in the process of CDT[17d]. The formation of H_2O_2 was confirmed from sono-induced bubble collapse[18]. Therefore, it is feasible to implement the ultrasound-mediated synergistic therapy by combining CO gas therapy with CDT.

Therefore, in this study, inspired by the band structure and Fenton-related ions, MIL-101(Cr)@CoOx nanoparticles were introduced to achieve ultrasound-mediated chemodynamic-gas therapy for the first time (**Scheme 1**). MIL-101(Cr) was prepared by a hydrothermal method and CoOx nanoparticles were armored homogeneously onto the surface of MIL-101(Cr) through two steps, ion-adsorption and sintering in N_2/H_2 atmosphere. MIL-101(Cr) can uptake CO_2 efficiently through the physical adsorption by dispersion interactions of the benzene ring with CO_2 molecules, and the chemical adsorption by the coordination between the metal sites and CO_2. The integration of CoOx and MIL-101(Cr) regulates the suitable band structure to achieve ultrasound-catalytic conversion of CO_2 to CO. The generated CO could induce mitochondrial dysfunction and produce more ROS to achieve gas therapy. Furthermore, with the existence of cobalt, MIL-101(Cr)@CoOx could also react with over-expressed intracellular H_2O_2 and trigger Fenton-like reaction to generate cytotoxic ·OH. Therefore, we hypothesized that with introduction of ultrasound, the therapeutic outcome of CDT could be amplified, primarily resulted from the ultrasonic cavitation-induced

conversion between Co^{3+} and Co^{2+}. Both the *in vitro* and *in vivo* studies were performed to test this novel ultrasound-mediated synergistic CO and CDT therapy for precise and effective tumor inhibition. This study aims to provide a distinctive concept to construct smart ultrasound-stimulus systems for minimally invasive and personalized cancer therapy with higher precisions.

2. Results and discussions

2.1 Characterization of MIL-101(Cr)@CoO$_x$

   MIL-101(Cr)@CoOx nanoparticles were synthesized via three steps of hydrothermal synthesis of MIL-101(Cr), Co ion adsorption and sintering in 5% H_2/N_2 atmosphere, as illustrated in Scheme 1. The as-prepared MIL-101(Cr) nanoparticles have an octahedron morphology with regular and smooth surface, and the particle size was 100-320 nm, as shown in scanning electron microscopy (SEM) images (**Figure S1**a-b, Supporting Information) and transmission electron microscopy (TEM) images at different magnifications (**Figure 1**a-b). After the loading of CoOx, MIL-101(Cr)@CoO$_x$ maintained the octahedron morphology but the surface become more rougher with embedded nanoparticles. No change of particle size was observed in MIL-101(Cr)@CoOx and the diameter of CoOx was ~5 nm. The high-resolution TEM observation (Figure 1c) presented the ordered lattice fringes of CoOx, and the measured lattice spacing between the adjacent lattice were 0.213 nm and 0.233 nm, which corresponding to (2 0 0) plane of CoO (JCPDS 43-1004) and (2 2 2) plane of Co_3O_4 (JCPDS 42-1467), respectively. The element distribution was analyzed using energy-dispersive X-ray spectroscopy (EDX). The distributions of C, O, Cr and Co elements were well matched with the MIL-101(Cr)@CoOx nanoparticles, and a homogenous distribution of Co onto MIL-101(Cr)@CoOx

was observed (Figure 1d).

X-ray diffraction (XRD) was used to analyze the crystallinities of MIL-101(Cr) and MIL-101(Cr)@CoOx (Figure 1e). The results confirmed that MIL-101(Cr) were highly crystallized and the characteristic diffraction peaks of MIL-101(Cr) at 5.88°, 8.46°, 9.08°, 10.36° and 16.56° were in good agreement with the data reported previously[19]. Compared with the XRD pattern of MIL-101(Cr), there is no changes in characteristic diffraction peaks of MIL-101(Cr)@CoOx, although the ratio of the intensities decreased slightly, and no peaks of CoOx were observed. The results suggest that the content of CoOx was relatively low to be detected, and the loading of CoOx did not affect the skeletal crystal structure of MIL-101(Cr), indicating that CoOx in the composites was well-dispersed.

The chemical composition and their valence states of MIL-101(Cr)@CoOx was further investigated by X-ray photoelectron spectroscopy (XPS). The chemical composition results (Figure 1f) agree well with those of EDX (Figure 1d), revealing the key elements of Co, Cr, O and C. The ratio of MIL-101(Cr) and CoOx in MIL-101(Cr)@CoOx was determined as 17:8. The Co 2p spectrum (Figure 1g) shows that Co $2p_{3/2}$ could be deconvoluted (Gaussian fitting) into two characteristic peaks located at 780.98 eV and 782.59 eV, which correspond with Co(III) and Co(II), respectively. The adjacent peaks represented the Co $2p_{3/2}$ satellites. The contents of Co(II) and Co(III) were calculated as ~50.7% and ~49.3%, respectively. For an experimental reference, pure CoOx nanoparticles were synthesized through calcining $Co(NO_3)_2 \cdot 6H_2O$ in N_2/H_2 atmosphere, using the same protocol of MIL-101(Cr)@CoOx. The results are shown in **Figure S2**, the particle size of CoOx is ~10 nm. The surface charges of MIL-101(Cr), MIL-101(Cr)@CoOx and CoOx nanoparticles were

also measured by ζ-potential analysis (**Figure S3**). The results indicate that the ζ-potential changes

from -8.7 mV to -6.2 mV after the *in-situ* growth of CoOx on the surface of MIL-101(Cr)@CoOx.

2.2 Functional characteristics of MIL-101(Cr)@CoOx.

The efficiency of MIL-101(Cr)@CoOx as a sono-catalyst to reduce CO_2 into CO was measured

using a hemoglobin (Hb) assay, as CO binds to iron center in hemoglobin and forms

carboxyhemoglobin (HbCO) complex[20]. Hb were bubbling with O_2 and CO to obtain HbO_2 and

HbCO complex and UV-Vis absorption before and after ultrasound treatments was compared. As

shown in **Figure S4**a-b, Hb alone showed two characteristics bands at 430 nm and 555 nm. The

absorbance of HbO_2 peaked at 405 nm, 541 nm and 576 nm, while HbCO complex showed the

absorption peaks of 420 nm, 535 nm and 568 nm. A clear colour change with formation of HbCO

complex is shown in Figure S4c. With the production of CO gas, the intensity of Hb at 430 nm and

555 nm decreased gradually while the absorbance of the other three bands at 420 nm, 535 nm and

568 nm increased, indicating the transformation from Hb to HbCO.

With subjected to the ultrasound treatment (1.0 MHz, 0.5 W/cm^2) for 1 to 5 min, the CO generation

for MIL-101(Cr)@CoOx increased, as shown in **Figure 2**a-c. The optical photographs showed the

instinct color change of the solution after ultrasound treatments, indicating the CO generation

intuitively (Figure 2c). The amount of CO release was quantified following the method reported

previously[21]. The amount of CO produced by MIL-101(Cr)@CoOx after 5 min US irradiation was

2.65 μM, which was significantly higher than all other control groups, 0.63 μM (Hb), 0.42 μM (Hb/

MIL-101(Cr)), and 0.93 μM (Hb/ CoOx), respectively. The data were shown in **Figure S5**a-c, **Figure**

S6a-c and **Figure S7**a-c. Without ultrasound irradiation, there is no CO generation from MIL-

101(Cr)@CoOx up to the 5 min treatment (**Figure S8**).

The CO_2 adsorption isotherms of MIL-101(Cr), MIL-101(Cr)@CoO$_x$ and CoO$_x$ at 37°C are shown in Figure 2d. CoOx exhibited very weak CO_2 capture, while MIL-101(Cr) and MIL-101(Cr)@CoOx showed considerable CO_2 adsorption capacity. The maximum CO_2 uptake at 1 bar and 37°C of MIL-101(Cr) and MIL-101(Cr)@CoOx were 30.62 cm^3 g^{-1} and 24.82 cm^3 g^{-1}, respectively. The adsorption capacity of MIL-101(Cr) MOF is attributed to the physical adsorption by dispersion interactions of the benzene ring with CO_2 molecules, and the chemical adsorption by the coordination between the metal sites and CO_2. The reduction in CO_2 adsorption comes down to CoOx growth in pores of MIL-101(Cr). It is well known that the CO_2 adsorption capacity decreases as the temperature increases[22]. The results showed the CO_2 capture ability of MIL-101(Cr)@CoOx (105 cm^3 g^{-1}) is better than that of many other reports such as Zn-DPA (44.5 cm^3 g^{-1}) and Mg-MOF-74 (33.9 cm^3 g^{-1}) at 1 atm and 273 K and it is beneficial for chemisorbing and activating CO_2 gas[19, 22-23].

The bandgaps of MIL-101(Cr) and MIL-101(Cr)@CoOx were 1.63 eV and 1.49 eV respectively, measured from the UV-Vis diffuse reflectance spectra (**Figure S9** and Figure 2e). It is clear that the loading of CoOx onto MIL-101(Cr) induced a decrease in bandgap of the MIL-101(Cr)@CoOx composite. The valence band positions for MIL-101(Cr) and MIL-101(Cr)@CoOx are 0.55 eV and 0.74 eV, respectively, measured from the valence band XPS (Figure 2f-g). To obtain the energy diagram versus the standard hydrogen electrode (SHE), the vacuum level of 4.5 eV is aligned at 0 eV[24]. Taking the work function of XPS instrument (4.62 eV) into account, the valence band maximum values for MIL-101(Cr) and MIL-101(Cr)@CoOx are 0.67 eV and 0.86 eV, respectively. The calculated bandgap is shown in Figure 2e, the minimum values of conduction band for MIL-

101(Cr) and MIL-101(Cr)@CoOx are -0.96 eV and -0.63 eV (Figure 2i), respectively. Based on these results, we speculate that the unique MIL-101(Cr) MOF structure can facilitate CO_2 adsorption and activation. The composite of CoOx with MIL-101(Cr) was able to adjust the bandgap structure and the conduction band position, energetically favorable to reduce CO_2 to CO. The mechanism of ultrasound-catalyzed CO generation by MIL-101(Cr)@CoOx is explained in Figure 2h-i.

To evaluate the Fenton activity of MIL-101(Cr)@CoOx, the production of hydroxyl radicals was determined using 3,3′,5,5′-tetramethylbenzidine (TMB) chromogenic method. In the presence of H_2O_2, Fenton reagents react with H_2O_2 to generate ·OH, which oxidizes TMB to ox-TMB, giving an aquamarine blue color with the characteristic peak at 653 nm. No absorption peak was observed on the UV-Vis absorbance spectrum of TMB solution (0.8 mM) after bubbling with CO gas (**Figure S10**), confirming CO is non-functional for the TMB chromogenic reaction.

The characteristic peaks of ox-TMB were observed with the presence of MIL-101(Cr)@CoOx and H_2O_2, while H_2O_2 alone and MIL-101(Cr)@CoOx alone did not elicit the chromogenic reaction, as shown in **Figure 3**a. The time-course absorbance of TMB (at 653 nm) with increasing H_2O_2 concentrations from 0.5 to 10 mM is shown in Figure 3b. The results confirmed that Fenton-like reaction by MIL-101(Cr)@CoOx was accelerated with the increase of H_2O_2 concentrations, demonstrated the H_2O_2-induced enhanced ·OH production. Electron spin resonance (ESR) spectroscopy was carried out to further confirm the type of generated ROS, 5,5-dimethyl-1-pyrroline N-oxide (DMPO) was used as a typical trapping agent for radical species. As shown in Figure 3c, there are four characteristic signals with a ratio of 1:2:2:1, which represents the DMPO-OH complex, thus indicating the generation of ·OH during the Fenton-like reaction.

We further studied the Fenton activity of MIL-101(Cr)@CoOx when subjected to ultrasound irradiation. Compared to the non-ultrasound treatment, the chromogenic reaction rate of the MIL-101(Cr)@CoOx + H_2O_2 + TMB group under the ultrasound irradiation is about two times higher (Figure 3d and **Figure S11**a-b), which indicating that a clear promotion in ·OH production in this system induced by ultrasound. To verify the above results, the sono-catalytic activity of MIL-101(Cr) and CoOx was compared, as shown in **Figure S12** and **Figure S13**. Regardless of the presence of ultrasound, MIL-101(Cr) did not show much catalytic activity, while CoOx exhibited a weak catalytic ability, which increased with the ultrasound duration time.

We have considered the existence of any thermal effect, and the structural and morphological changes of MIL-101(Cr)@CoOx after subjecting to ultrasound irradiation. With increasing sonication time, the temperature increases of MIL-101(Cr)@CoOx solution were not distinguishable from that of deionized water (**Figure S14**). Notably, the content of Co^{2+} increased significantly, from ~50.7% to ~69.7%, while Co^{3+} decreased from ~49.3% to ~30.3% after 5 min ultrasound irradiation (Figure 3e), indicating that MIL-101(Cr)@CoOx facilitated Co^{2+}-engaged Fenton-like reaction, thus confirming the catalytic mechanism of the sono-Fenton system of MIL-101(Cr)@CoOx. Co concentration in supernatant of MIL-101(Cr)@CoOx after ultrasound irradiation increased from 75 ppm to 84 ppm (Figure 3f), as expected. A fraction of small nanoparticles (marked in red circles) with a diameter of 10-20 nm was also observed after sonication (**Figure S15**), which implied CoOx shed from MIL-101(Cr)@CoOx composites.

2.3 *In vitro* study

In vitro cell biocompatibility and the therapeutic efficacy of MIL-101(Cr)@CoOx were evaluated

using a mouse hepatocytes AML12 cell line and a 4T1 mouse breast cancer cell line. Methyl thiazolyl

tetrazolium (MTT) assay showed that MIL-101(Cr)@CoOx had no obvious toxicity to AML12 cells

(**Figure 4**a), with the concentrations up to 100 ppm, there was no statistical differences in the cell

viability. The up-limit of non-toxic concentration of H_2O_2 was also determined, which is 30 μM for

4T1 cells (**Figure S16**). The cell viability of 4T1 cells in the presence of MIL-101(Cr)@CoOx, MIL-

101(Cr)@CoOx/H_2O_2, MIL-101(Cr)@CoOx/US and MIL-101(Cr)@CoOx/H_2O_2/US was compared.

As shown in Figure 4b, MIL-101(Cr)@CoOx exhibited concentration-dependent cytotoxicity to 4T1

cells, the killing effect was significantly enhanced in the combination with H_2O_2 due to the H_2O_2-

dependent Fenton-like reaction. The introduction of ultrasound further enhanced cytotoxicity to 4T1

cells, confirming a higher efficiency of MIL-101(Cr)@CoOx as a suitable agent to promote sono-

Fenton activity and sono-induced CO gas therapy.

To further verify the role of MIL-101(Cr)@CoOx in the inhibition of cell growth, the cell viability

of 4T1 cells when treated only with MIL-101(Cr) or CoOx was compared. There is no clear inhibition

effect for both MIL-101(Cr) alone and CoOx alone groups. A statistically significant promotion of

killing was noticed in CoOx treated with ultrasound irradiation (Figure 4c and **Figure S17**). The most

notable cytotoxicity was found in MIL-101(Cr)@CoOx + H_2O_2 + US groups. The Co content in 4T1

cells after incubated with MIL-101(Cr)@CoOx for different time (2 h, 4 h and 8 h) was measured by

ICP analysis (Figure S18). The result indicated that the Co concentration increased with the

incubation time, indicating that MIL-101(Cr)@CoOx could be effectively taken up by the cells.

The cell viability for MIL-101(Cr)@CoOx with/without the addition of H_2O_2 and US was also

compared with other test/control groups by staining with Calcein-AM & PI. As shown in Figure 4d,

the Live / Dead assay results supported those from MTT assay. Among all the test groups and in comparison with other groups without the addition of H_2O_2 or US, the strongest red fluorescence (indicating dead cells) and those of weakest green fluorescence (indicating live cells) were observed in MIL-101(Cr)@CoOx + H_2O_2 + US group, thus indicating the enhanced capability in inducing cell apoptosis for MIL-101(Cr)@CoOx.

To understand the mechanism of MIL-101(Cr)@CoOx to promote *in vitro* anticancer activity, a series of assays were carried out to study the intracellular activities of 4T1 cells subjected to various treatments, with/without ultrasound (and H_2O_2). The intracellular CO generation was measured using a fluorescence carbon monoxide probe CAY10733. Based on the Pd0-mediated Tsuji-Trost reaction, CAY10733 could release 2,7-dichlorofluorescein (DCF) in the presence of CO. It was found that a strong green fluorescence representing DCF was observed when the cells were co-incubated with MIL-101(Cr)@CoOx and irradiated with US, indicating the notable sono-catalyzed CO production ability of MIL-101(Cr)@CoOx (**Figure 5**a). The cells of the other five groups showed negligible fluorescence.

CO can directly cause mitochondrial dysfunction, reduce energy and facilitate ROS production. 2′,7′-dichlorofluorescein diacetate (DCFH-DA) was used for ROS detection, which could be uptaken by live cells, converted to DCF and emitting green fluorescence due to oxidation. As shown in Figure 5b, a limited ROS generation was observed in control and US alone groups, and the cells treated with MIL-101(Cr)@CoOx displayed moderate green fluorescence, indicating the formation of ROS, and attributed towards chemodynamic therapy. Notably, the introduction of H_2O_2 or US induced a significant enhancement in the green fluorescence intensity. The highest ROS level was observed

when combing MIL-101(Cr)@CoOx with H_2O_2 and US together, suggesting the most production of

·OH and aggravated oxidative stress in the cells. The phenomenon was caused by the combination of

CO-promoted ROS generation and sono-Fenton effect. In addition, the intracellular GSH level was

examined qualitatively using a fluorescence probe naphthalene-2,3-dicarboxaldehyde (NDA) (Figure

S19) and quantitatively using 5,5'-dithiobis-(2-nitrobenzoic acid) (DTNB) (Figure S20), respectively.

The results demonstrated that MIL-101(Cr)@CoOx + H_2O_2 + US group exhibited lowest intracellular

GSH level and induced the most intracellular oxidative stress, which agrees well with the ROS level

after different treatments.

As the main cellular organelle for energy supply, mitochondria play an important role in regulating

cell life. A fluorescent probe JC-1 was used to detect the change of mitochondrial membrane potential

(MMP) of cells. JC-1 intends to aggregate in the matrix of mitochondrial and form J-aggregates in

healthy mitochondrial with high MMP. However, JC-1 could not aggregate in the matrix of

mitochondrial and exist in the form of monomer in damaged mitochondrial with low MMP. J-

aggregates and J-monomers produce red and green fluorescence, respectively. As shown in Figure 5d,

moderate green fluorescence was observed in the MIL-101(Cr)@CoOx-treated cells, indicating the

certain mitochondrial transmembrane potential depolarization and mitochondrial damage due to the

·OH production by Fenton-like reaction. After being treated with MIL-101(Cr)@CoOx and

ultrasound, the green fluorescence of JC-1 monomers was greatly increased and the red fluorescence

of JC-1 aggregates was decreased in the 4T1 cells, suggesting that generated CO and ROS

cooperatively exacerbated mitochondrial dysfunction. The other groups showed strong red

fluorescence in the cells. To confirm the CO generation and mitochondrial dysfunction, the

intracellular ATP level was also measured using an ATP assay. The ATP level in MIL-101(Cr)@CoOx + US group showed a significant reduction compared to the other three groups (Figure 5c), as expected.

Overall, all *in vitro* cellular results demonstrated that by combining MIL-101(Cr)@CoOx with ultrasound irradiation, a highly promising ultrasound-induced CO gas therapy & chemodynamic therapy has been developed for inducing and promoting cancer cell apoptosis, which has a potential synergy for improved cancer treatment.

2.4 *In vivo* antitumor study

To further evaluate the *in vivo* antitumor properties of MIL-101(Cr)@CoOx, an 4T1 mouse tumor model was used. The *in vivo* distribution of Co content in different organs (heart, liver, spleen, kidney and tumor) after i.v. injection of MIL-101(Cr)@CoOx at different time points (6 h, 12 h, 24 h and 48 h) was investigated by ICP-OES. As shown in Figure S21, the retention of MIL-101(Cr)@CoOx in liver, spleen and tumors increased over time, with a high level of accumulation in tumors within 12-24 h. While at 48 h post injection, the metabolism and clearance effect induced the decrease of MIL-101(Cr)@CoOx in these organs. Subsequently, the tumor-bearing nude mice were randomly divided into 6 groups (1) Control (physiological saline solution); (2) US alone (1.0 MHz, 1.5 W cm^{-2}, 2 min); (3) MIL-101(Cr) + US (17 mg kg^{-1}, i.v. injection); (4) CoOx + US (8 mg kg^{-1}, i.v. injection); (5) MIL-101(Cr)@CoOx (25 mg kg^{-1}, i.v. injection) and (6) MIL-101(Cr)@CoOx + US (25 mg kg^{-1}, i.v. injection). The injection was repeated at 5th day and 10th day (**Figure 6**a). Ultrasound irradiation treatments were performed at 12 h and 24 h after intravenously injection of test samples. The body weight of mice and the tumor size were closely monitored during the whole testing period.

As shown in **Figure S22**, no discernible difference was observed among the six groups, indicating the treatments were safe and did not affect the health of the mice. It is clear that compared with other five groups, the tumor growth of MIL-101(Cr)@CoOx + US group (Group 6) was significantly inhibited during the 14-day testing period (Figure 6b), and the tumor regression rate was about ~86.4%, demonstrating the super tumor inhibition effect by combining ultrasound-induced CO therapy and CDT. After completing the treatments, the mice were sacrificed and the subcutaneous tumors were excised, collected, weighed and photographed (Figure 6c-d). The variations of tumor weight and the representative photographs of tumors were all in agreement.

The therapeutic performance of MIL-101(Cr)@CoOx + US treatment was also confirmed by hematoxylin−eosin (H&E) and Ki67 staining. As shown in Figure 6e, numerous nuclear pyknosis and severe cytoplasmic vacuolization were observed from H&E staining, and the most Ki67-positive cells were found in MIL-101(Cr)@CoOx + US group (Group 6). The results demonstrated that MIL-101(Cr)@CoOx with ultrasound irradiation induced cell apoptosis and inhibited the cell proliferation exceptionally.

To further verify the biosafety of MIL-101(Cr)@CoOx, the blood biochemistry and hematological analysis of the mice were carried out at 1 day, 3 days and 7 days after injections. No abnormalities and obvious side effects were founded. As shown in **Figure S23**, there are no significant differences in the levels of alanine aminotransferase (ALT), aspartate aminotransferase (AST), white blood cell (WBC), red blood cell (RBC), blood platelet (PLT), hemoglobin (HGB), mean corpuscular hemoglobin concentration (MCHC), mean corpuscular hemoglobin (MCH) and mean corpuscular volume (MCV). To evaluate the tissue toxicity of MIL-101(Cr)@CoOx, histological examination of

major organs, including heart, liver, spleen, lung and kidney was performed. There is no evidence of tissue damage after various treatments, all showed the negative results (Figure 6f). Therefore, a good biocompatibility and biosafety of MIL-101(Cr)@CoOx was confirmed.

3. Conclusion

In summary, for the first time, we introduced and synthesized MIL-101(Cr)@CoOx nanoparticles to enable ultrasound-mediated CO gas therapy and chemodynamic therapy. By successfully integrating the unique MOF structure of MIL-101(Cr) with the specific band structure CoOx, MIL-101(Cr)@CoOx has exhibited a substantial CO_2 adsorption capacity, while sonocatalyzing CO_2 to CO make it feasible to combine CO gas therapy with chemodynamic therapy for a new synergetic Ultrasound-Assisted Chemodynamic-Gas (UACG) Cancer Therapy. Our results confirmed that MIL-101(Cr)@CoOx showed Fenton activity, attributed to the Cobalt-engaged Fenton-like reaction. Ultrasound further induced the changes of the valence states of Co^{3+} to Co^{2+}, thus leading to a distinct promotion in ·OH production, and presenting a desired sono-catalytic Fenton activity. Both the *in vitro* and *in vivo* study demonstrated that MIL-101(Cr)@CoOx with ultrasound irradiation exhibited superior capability in suppressing the proliferation and growth of mouse 4T1 breast cancer cells and breast tumor by the synergism of CO gas therapy and chemodynamic therapy. This study therefore extended the development of the ultrasound application to catalyze potential therapeutic platform to achieve synergetic cancer therapy.

Supporting Information

Supporting Information is available online or from the author.

Conflict of Interest

The authors declare no conflict of interest.

References

[1] M. Yuan, S. Liang, L. Yang, F. Li, B. Liu, C. Yang, Z. Yang, Y. Bian, P. a. Ma, Z. Cheng, J. Lin, *Adv. Mater.* **2023**, 35, 2209589.

[2] a) J. Chai, J. Zhu, Y. Tian, K. Yang, J. Luan, Y. Wang, *J. Mater. Chem. B* **2023**, 11, 1849; b) S. Garcia-Gallego, G. J. L. Bernardes, *Angew. Chem., Int. Ed.* **2014**, 53, 9712; c) T.-Y. Wang, X.-Y. Zhu, F. G. Wu, *Bioact. Mater.* **2023**, 23, 129.

[3] a) L. Yu, P. Hu, Y. Chen, *Adv. Mater.* **2018**, 30, 1801964; b) S. Cheng, D. Enserro, V. Xanthakis, L. M. Sullivan, J. M. Murabito, E. J. Benjamin, J. F. Polak, C. J. O'Donnell, P. A. Wolf, G. T. O'Connor, J. F. Keaney, R. S. Vasan, *Eur. Heart J.* **2014**, 35, 2980.

[4] a) Y. Li, J. Dang, Q. Liang, L. Yin, *ACS Cent. Sci.* **2019**, 5, 1044; b) J. J. Rose, L. Wang, Q. Xu, C. F. McTiernan, S. Shiva, J. Tejero, M. T. Gladwin, *Am. J. Respir. Crit. Care Med.* **2017**, 195, 596; c) T. Zhai, W. Zhong, Y. Gao, H. Zhou, Z. Zhou, X. Liu, S. Yang, H. Yang, *ACS Appl. Mater. Interfaces*

2021, 13, 39100.

[5] a) W. Fan, N. Lu, Z. Shen, W. Tang, B. Shen, Z. Cui, L. Shan, Z. Yang, Z. Wang, O. Jacobson, Z. Zhou, Y. Liu, P. Hu, W. Yang, J. Song, Y. Zhang, L. Zhang, N. M. Khashab, M. A. Aronova, G. Lu, X. Chen, *Nat. Commun.* **2019**, 10, 1241; b) B. Wegiel, D. Gallo, E. Csizmadia, C. Harris, J. Belcher, G. M. Vercellotti, N. Penacho, P. Seth, V. Sukhatme, A. Ahmed, P. P. Pandolfi, L. Helczynski, A. Bjartell, J. L. Persson, L. E. Otterbein, *Cancer Res.* **2013**, 73, 7009.

[6] X. Yao, P. Yang, Z. Jin, Q. Jiang, R. Guo, R. Xie, Q. He, W. Yang, *Biomaterials* **2019**, 197, 268.

[7] S.-B. Wang, C. Zhang, J.-J. Ye, M.-Z. Zou, C.-J. Liu, X.-Z. Zhang, *ACS Cent. Sci.* **2020**, 6, 555.

[8] a) Y. Wang, D. Jing, J. Yang, S. Zhu, J. Shi, X. Qin, W. Yin, J. Wang, Y. Ding, T. Chen, B. Lu, Y. Yao, *Acta Biomater.* **2022**, 154, 467; b) W.-P. Li, C.-H. Su, L.-C. Tsao, C.-T. Chang, Y.-P. Hsu, C.-S. Yeh, *ACS Nano* **2016**, 10, 11027; c) U. Hasegawa, A. J. van der Vlies, E. Simeoni, C. Wandrey, J. A. Hubbell, *J. Am. Chem. Soc.* **2010**, 132, 18273.

[9] a) M. Ding, H. Chen, T. Wang, L. Wu, K. Shao, L. Han, X. Kong, J. Shi, *Chem. Eng. J.* **2023**, 456, 141091; b) D.-W. Zheng, B. Li, C.-X. Li, L. Xu, J.-X. Fan, Q. Lei, X.-Z. Zhang, *Adv. Mater.* **2017**, 29, 1703822.

[10] L. Huang, L. Zeng, Y. Chen, N. Yu, L. Wang, K. Huang, Y. Zhao, G. Han, *Nat. Commun.* **2021**, 12, 122.

[11] F. Yang, J. Dong, Z. Li, Z. Wang, *ACS Nano* **2023**, 17, 4102.

[12] a) G. Li, H. Lei, Y. Yang, X. Zhong, F. Gong, Y. Gong, Y. Zhou, Y. Zhang, H. Shi, Z. Xiao, Z. Dong, L. Cheng, *Adv. Sci.* **2022**, 9, 2201069; b) K. Song, J. Du, X. Wang, L. Zheng, R. Ouyang, Y. Li, Y. Miao, D. Zhang, *Adv. Healthcare Mater.* **2022**, 11, 2102503; c) M. Zhang, D. Yang, C. Dong,

H. Huang, G. Feng, Q. Chen, Y. Zheng, H. Tang, Y. Chen, X. Jing, *ACS Nano* **2022**, 16, 9938.

[13] C. Jia, Y. Guo, F.-G. Wu, *Small* **2022**, 18, 2103868.

[14] a) J. Meng, Z. Jin, P. Zhao, B. Zhao, M. Fan, Q. He, *Sci. Adv.* **2020**, 6, eaba1362; b) F. Yang, W. Yu, Q. Yu, X. Liu, C. Liu, C. Lu, X. Liao, Y. Liu, N. Peng, *Small* **2023**, 19, 2206124.

[15] L. Ma, H. Huang, W. Feng, L. Chen, L. Xia, Y. Yu, J. Wang, Y. Chen, *Adv. Funct. Mater.* **2022**, 32, 2208220.

[16] a) S.-L. Li, P. Jiang, F.-L. Jiang, Y. Liu, *Adv. Funct. Mater.* **2021**, 31, 2100243; b) J. Ruan, H. Liu, B. Chen, F. Wang, W. Wang, Z. Zha, H. Qian, Z. Miao, J. Sun, T. Tian, Y. He, H. Wang, *ACS Nano* **2021**, 15, 11428.

[17] a) Y. He, S. Guo, Y. Zhang, Y. Liu, H. Ju, *Biomaterials* **2021**, 275, 120962; b) Y. Li, R. Jia, H. Lin, X. Sun, F. Qu, *Adv. Funct. Mater.* **2021**, 31, 2008420; c) D. Jana, D. Wang, A. K. Bindra, Y. Guo, J. Liu, Y. Zhao, *ACS Nano* **2021**, 15, 7774; d) S. Liang, X. Xiao, L. Bai, B. Liu, M. Yuan, P. a. Ma, M. Pang, Z. Cheng, J. Lin, *Adv. Mater.* **2021**, 33, 2100333.

[18] N. H. Ince, G. Tezcanli, R. K. Belen, I. G. Apikyan, *Appl. Catal., B* **2001**, 29, 167.

[19] Y. Ma, J. Du, Y. Fang, X. Wang, *Chemsuschem* **2021**, 14, 946.

[20] I. H. Jain, L. Zazzeron, O. Goldberger, E. Marutani, G. R. Wojtkiewicz, T. Ast, H. Wang, G. Schleifer, A. Stepanova, K. Brepoels, L. Schoonjans, P. Carmeliet, A. Galkin, F. Ichinose, W. M. Zapol, V. K. Mootha, *Cell Metab.* **2019**, 30, 824.

[21] Z. Jin, Y. Wen, L. Xiong, T. Yang, P. Zhao, L. Tan, T. Wang, Z. Qian, B.-L. Su, Q. He, *Chem. Commun.* **2017**, 53, 5557.

[22] P. Wu, Y. Li, J.-J. Zheng, N. Hosono, K.-i. Otake, J. Wang, Y. Liu, L. Xia, M. Jiang, S. Sakaki, S.

Kitagawa, *Nat. Commun.* **2019**, 10, 4362.

[23] a) O. Shekhah, Y. Belmabkhout, Z. Chen, V. Guillerm, A. Cairns, K. Adil, M. Eddaoudi, *Nat. Commun.* **2014**, 5, 4228; b) D. Kim, J. Park, Y. S. Kim, M. S. Lah, *Sci. Rep.* **2017**, 7.

[24] L. H. Li, T. Tian, Q. Cai, C.-J. Shih, E. J. G. Santos, *Nat. Commun.* **2018**, 9, 1271.
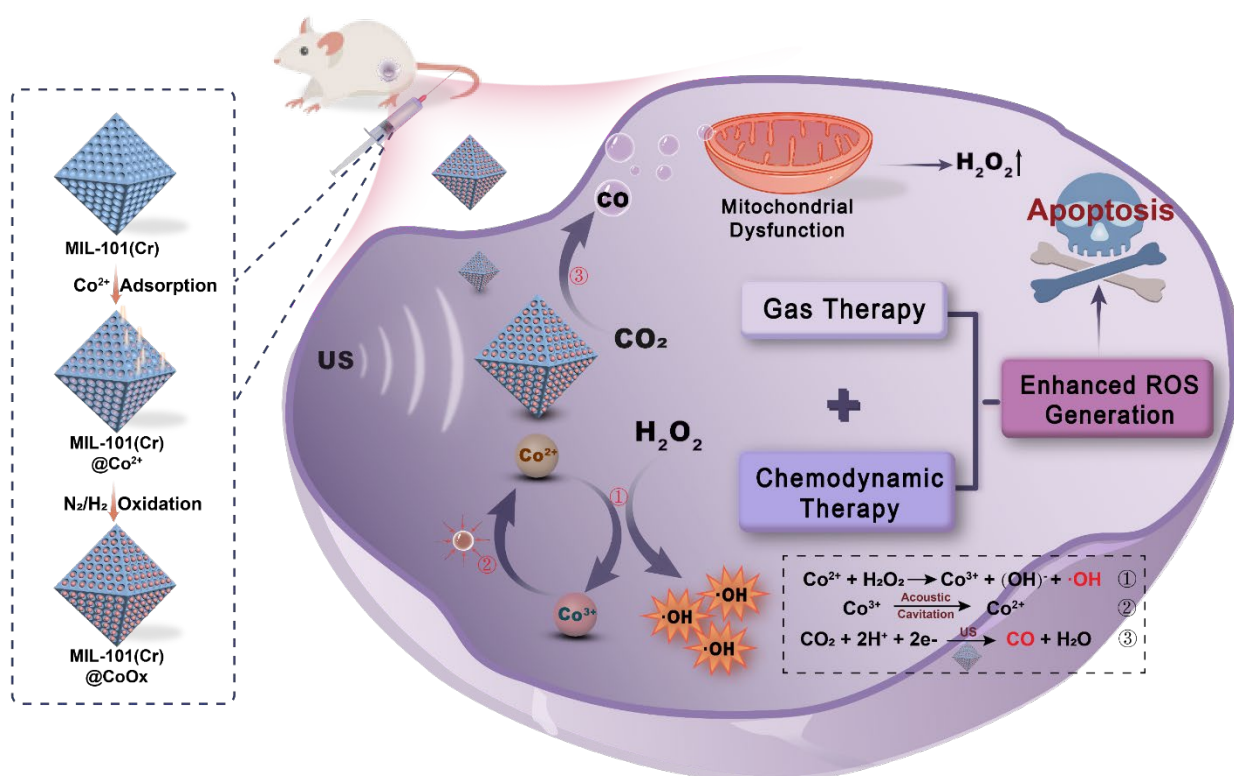
Scheme 1. Schematic illustration of the synthesis protocol of MIL-101(Cr)@CoOx and the therapeutic phenomenon of combination therapy.
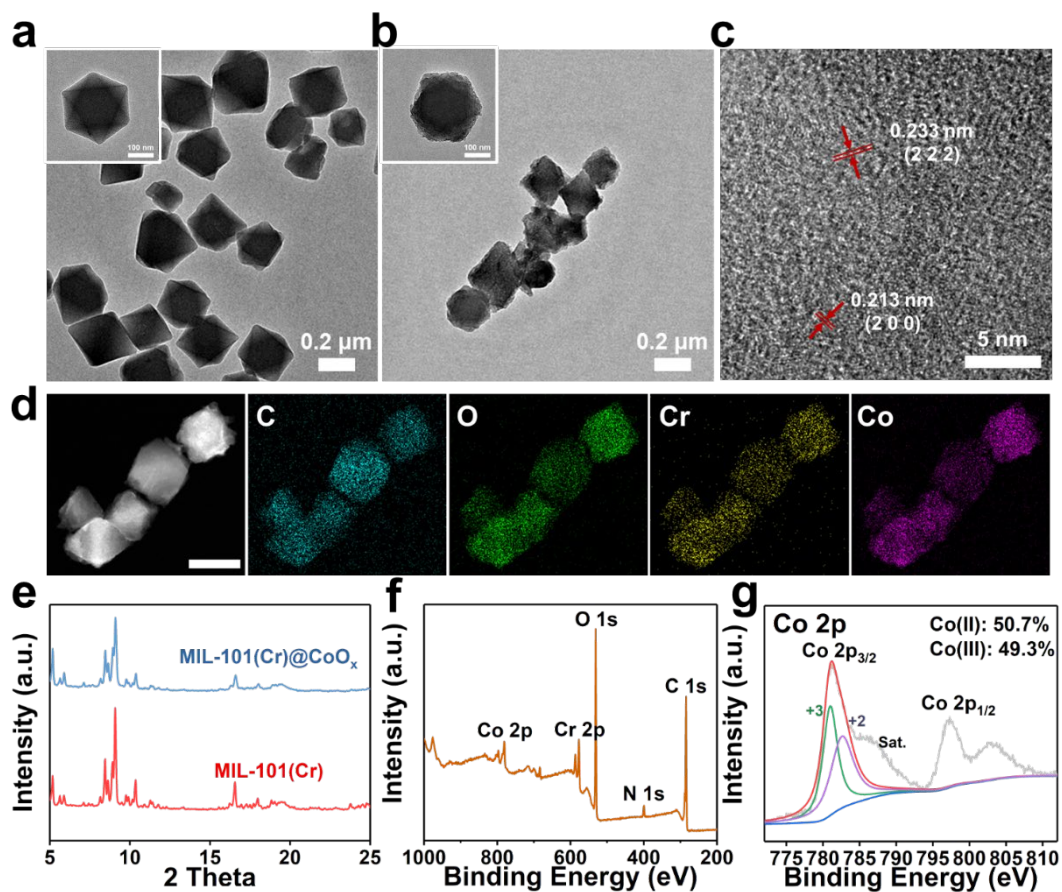
WILEY-VCH

Figure 1. Structure and morphology Characterization of MIL-101(Cr) and MIL-101(Cr)@CoOx. Transmission electron microscopy (TEM) images of (a) MIL-101(Cr) and (b) MIL-101(Cr)@CoOx (inner: high magnification). (c) High-resolution TEM image of MIL-101(Cr)@CoOx. (d) Energy-dispersive X-ray spectroscopy (C, O, Cr and Co) of MIL-101(Cr)@CoOx (scale bar: 100 nm). (e) XRD patterns of MIL-101(Cr) and MIL-101(Cr)@CoOx. (f) XPS spectra and (g) Co 2p XPS spectra of MIL-101(Cr)@CoOx.
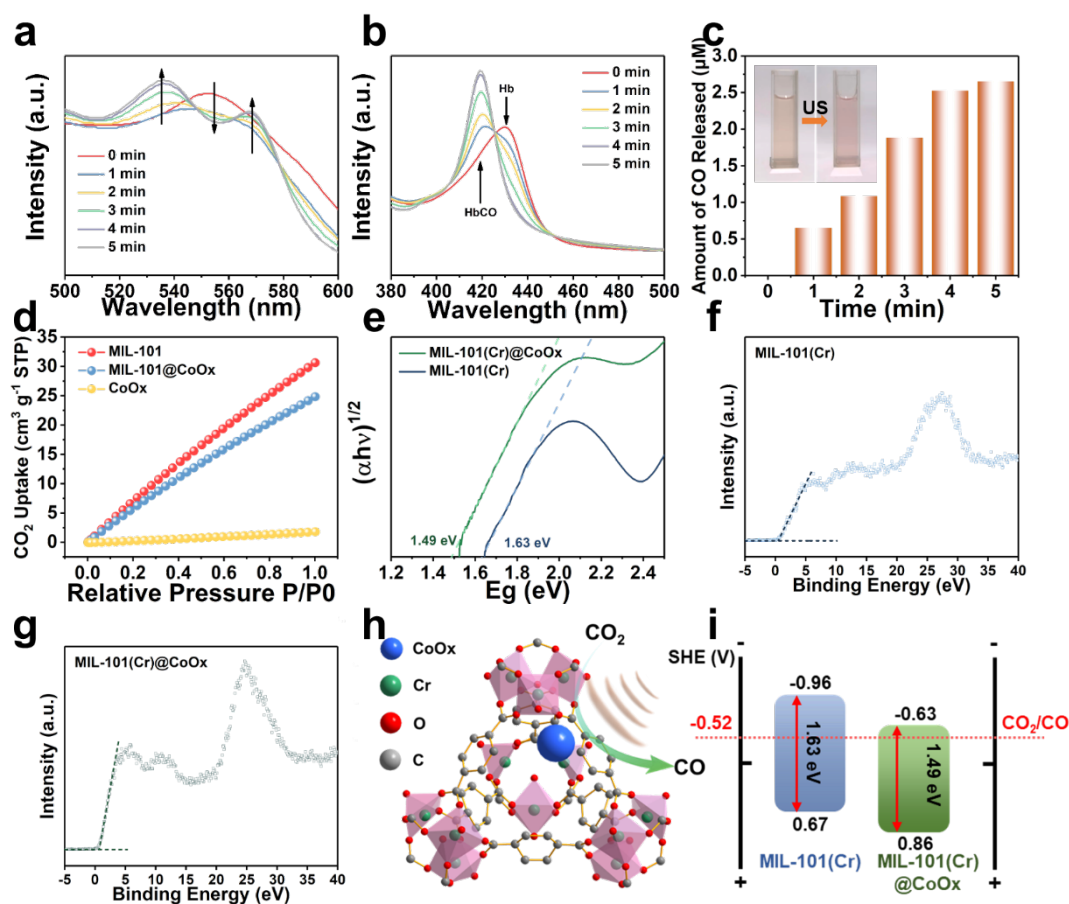
Figure 2. (a-b) UV-Vis absorption spectra of Hb (4.2 μM)/MIL-101(Cr)@CoOx mixture with different ultrasonic vibration time (1.0 MHz, 0.5 W cm^{-2}) for detecting CO generation by a hemoglobin (Hb) method. (c) The quantitative content of CO release under ultrasound irradiation (inner: the optical photographs of Hb/MIL-101(Cr)@CoOx before (left) and after (right) ultrasound irradiation). (d) CO$_2$ adsorption capacity of MIL-101(Cr), MIL-101(Cr)@CoOx and CoOx at 37°C. (e) Relationship between (αhν)$^{1/2}$ and Eg of MIL-101(Cr) and MIL-101(Cr)@CoOx. XPS high resolution valence band spectrum of (f) MIL-101(Cr) and (g) MIL-101(Cr)@CoOx. (h) The mechanism of ultrasound-catalyzed CO generation by MIL-101(Cr)@CoOx. (i) Energy diagram of MIL-101(Cr) and MIL-101(Cr)@CoOx.
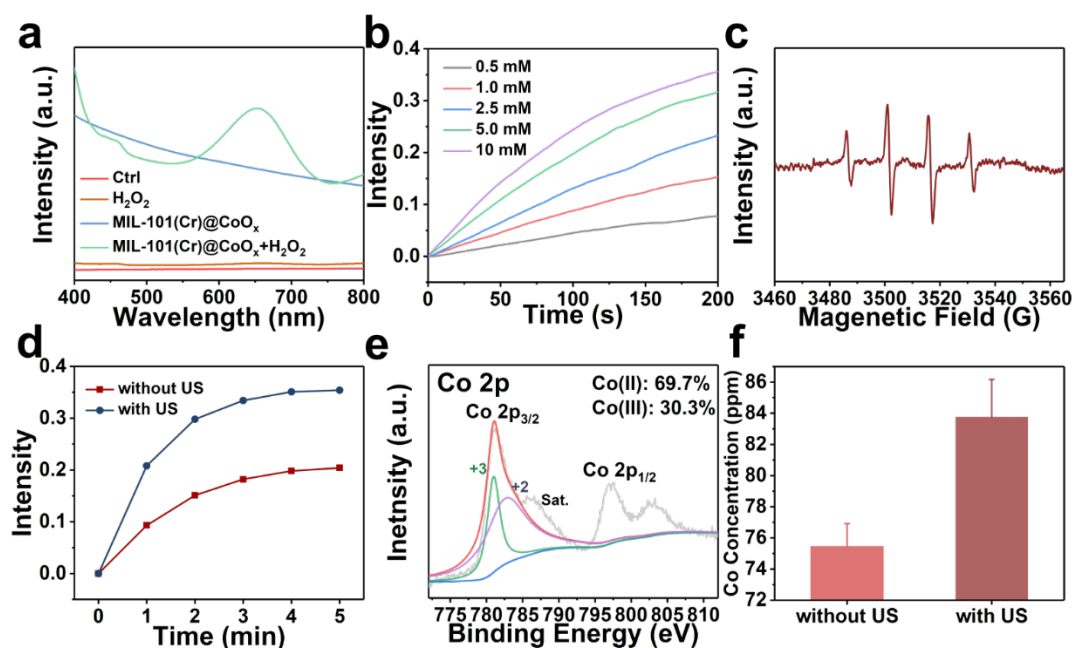
Figure 3. The sono-Fenton reaction of MIL-101(Cr)@CoOx. (a) UV-Vis absorbance spectra of TMB solution (0.8 mM) with the addition of MIL-101@CoOx (100 μg ml^{-1}), H_2O_2 (1mM) and MIL-101(Cr)@CoOx + H_2O_2. (b) Time-course absorbance at 653 nm at different H_2O_2 concentrations (0.5, 1.0, 2.5, 5.0 and 10 mM) with the addition of TMB and MIL-101(Cr)@CoOx. (C) ESR spectra of DMPO-OH in the presence of MIL-101(Cr)@CoOx and H_2O_2. (d) Time-dependent intensity changes at 653 nm of TMB in the presence of MIL-101(Cr)@CoOx and H_2O_2 with or without US irradiation (1.0 MHz, 1.0 W cm^{-2}). (e) Co 2p XPS spectra of MIL-101(Cr)@CoOx after US irradiation (1.0 MHz, 1.0 W cm^{-2}, 5 min). (f) Co concentration in the supernatant of MIL-101(Cr)@CoOx solution before and after ultrasound irradiation by ICP-OES.
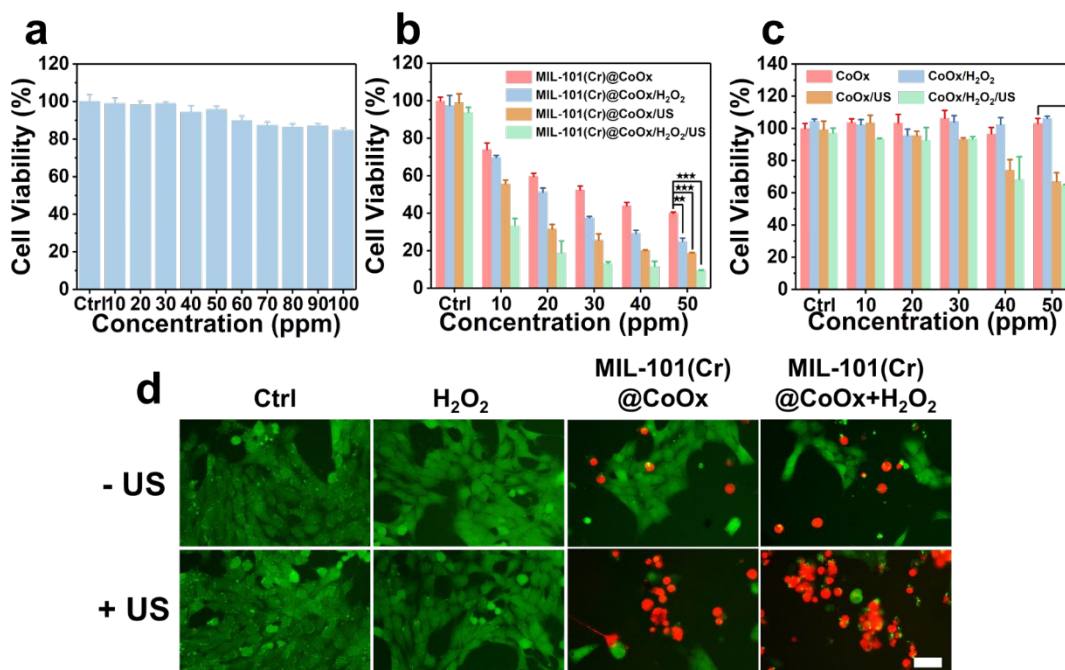
Figure 4. (a) Cell viability of AML12 cells after incubated with MIL-101(Cr)@CoOx with different concentrations. (b) Cell viability of 4T1 cells after incubated with MIL-101(Cr)@CoOx, MIL-101(Cr)@CoOx/H_2O_2, MIL-101(Cr)@CoOx/US and MIL-101(Cr)@CoOx/H_2O_2/US (1.0 MHz, 1.0 W cm^{-2}, 3 min). (c) Cell viability of 4T1 cells after incubated with CoOx, CoOx/H_2O_2, CoOx/US and CoOx/H_2O_2/US. (d) Fluorescence images of 4T1 cells stained with Calcein-AM & PI under different treatments. Scale bar is 200 μm. ***$p < 0.001$, **$p < 0.01$, *$p < 0.05$.
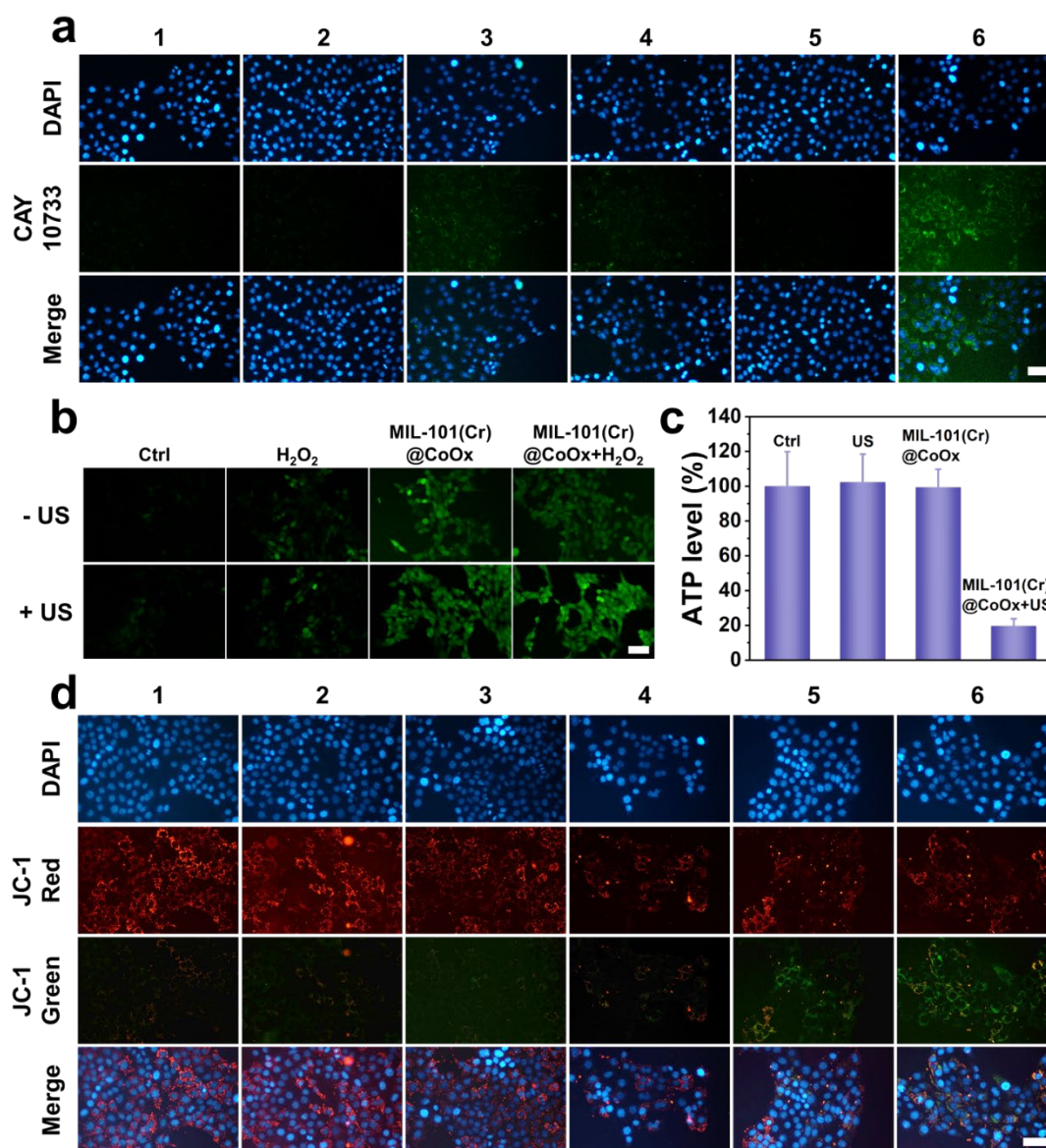
Figure 5. (a) Fluorescence images of 4T1 cells stained with DAPI for marking nuclei and CAY10733 for the detection of intracellular CO level. Scale bar is 100 μm. (b) Fluorescence images of 4T1 cells stained with DCFH-DA under different treatments. Scale bar is 100 μm. (c) The ATP level in 4T1 cells with different treatments. (d) Mitochondrial membrane potential measured in 4T1 cells by JC-1 probe. Scale bar is 100 μm. 1: Control; 2: US; 3: MIL-101(Cr) + US; 4: CoOx + US; 5: MIL-101(Cr)@CoOx; 6: MIL-101(Cr)@CoOx +US.
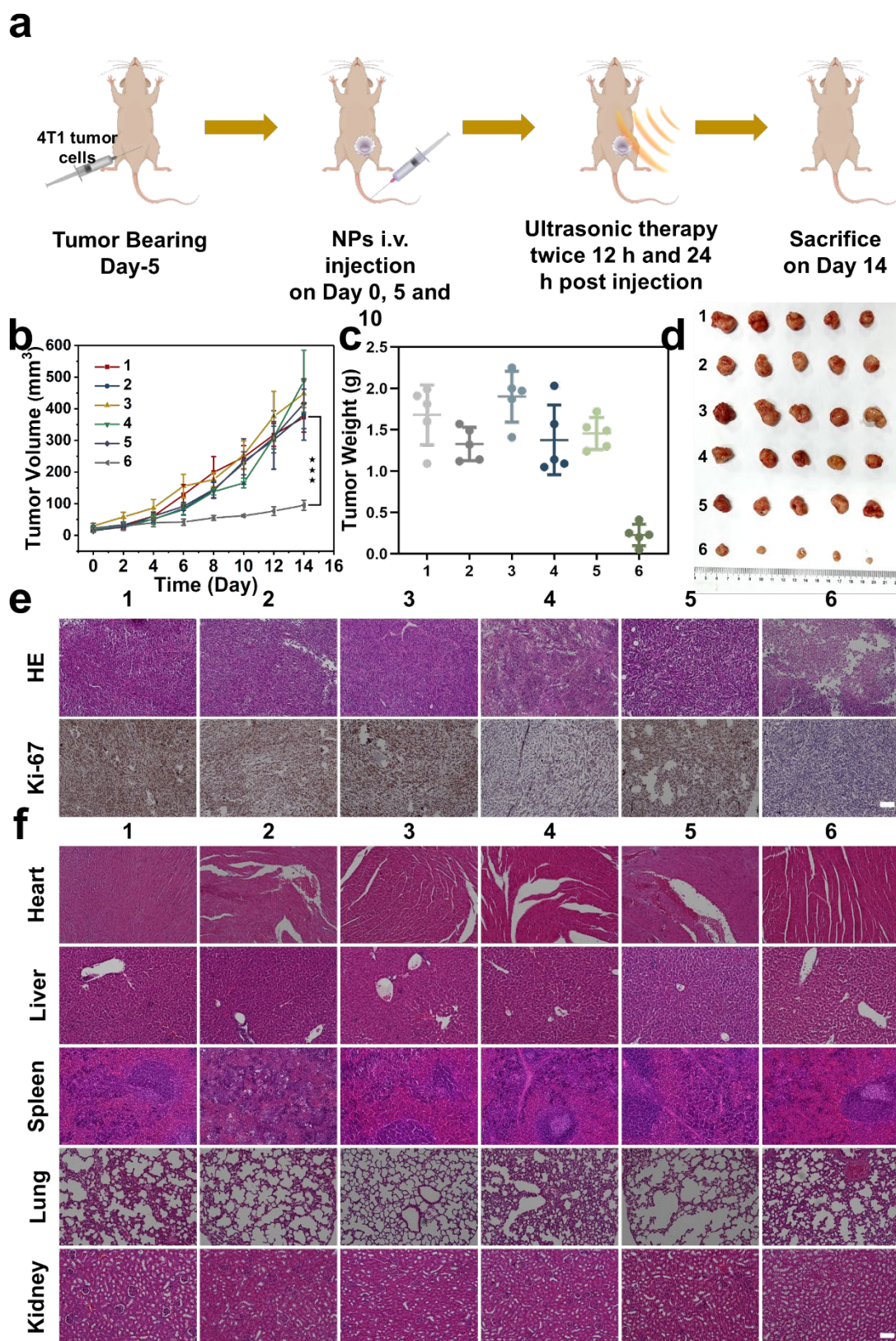
Figure 6. *In vivo* antitumor study. (a) Schematic illustration of *in vivo* experiments. (b) The change

curve of tumor volume of mice with different treatments (n = 5, mean ± SD). ***p < 0.001, **p <

0.01, *p < 0.05. (c) Tumor weight and (d) photographs of tumors collected from mice after (day 14) different treatments (n = 5, mean ± SD). (e) HE and Ki67 staining of tumors collected from mice after (day 14) different treatments. Scale bar is 100 μm. (f) HE staining of main organs (heart, liver, spleen, lung and kidney) collected from mice after (day 14) different treatments. Scale bar is 100 μm. 1: Control; 2: US; 3: MIL-101(Cr) + US; 4: CoOx + US; 5: MIL-101(Cr)@CoOx; 6: MIL-101(Cr)@CoOx +US.